www.afm-journal.d

Atomic Insights for Optimum and Excess Doping in Photocatalysis: A Case Study of Few-Layer Cu-ZnIn₂S₄

Pengfei Wang, Zhurui Shen, Yuguo Xia, Haitao Wang, Lirong Zheng, Wei Xi, and Sihui Zhan*

Herein, an example of Cu-doped few-layer ZnIn₂S₄ nanosheets is used to reveal the origin of optimum and excess doping for photocatalysts at atomic level. Results show that the metal-S4 coordination maintains well with 0.5 wt% Cu substituted Zn atoms in the lattice. The introduced Cu atoms bring electronic acceptor states close to the valence band (VB) maximum and thus ensures higher charge density and efficient carrier transport, resulting in an optimum hydrogen evolution rate of 26.2 mmol h⁻¹ g⁻¹ and an apparent quantum efficiency of 4.76% at 420 nm. However, a distorted atomic structure and largely upshift of VB maximum with Cu-S_{3.6} coordination are found with excess doping concentration (3.6 wt%). These bring the heavy charge recombination and consequentially dramatic reduced activity. This work provides a new insight into elemental doping study and takes an important step toward the development of ultrathin 2D photocatalysts.

1. Introduction

Photocatalysis has been regarded as one of the most appealing strategies to overcome the energy and environmental crisis.^[1-4] However, the activity of photocatalysts has long been restricted by the narrow solar light response range and low efficiency of charge separation/transfer.[1-11] The former is obvious in the wide-bandgap photocatalysts, for example, TiO2, [5,6] while the latter is obvious in the narrow-bandgap photocatalysts, for example, g-C₃N₄ and metal sulfide.^[9,10] To solve these two problems, doping, especially using external heteroatoms, has been widely used. [6-11] For one thing, the heteroatom can form the intermediate states in the gap, and effectively expand the response range of solar light.[6-8] For another, the change of electronic structure by the dopants and/or the charge characteristic of dopants (e.g., metal cations) themselves would greatly promote the charge separation/transfer.[9,10] These have brought great progress for improving the traditional photocatalysts. However, the vital drawback of doping is, via atomic substitution or existing in the interstitial site, the doping of heteroatom will inevitably change the atomic structure of photocatalyst and possibly form some recombination centers.[9,10] This will reduce the advantages of doping, and excess doping (always still a small fraction) can even cause decline in the activity photocatalyst. Therefore, besides

designing novel doping methods, for example, the recent noninvasively doping strategy,[11] it is important to study the atomic origin of optimum doping using the latest techniques and theoretical methods. [9,10] This will bring an in-depth understanding of its functional mechanism and a rational design of highly active doping photocatalysts. Meanwhile, although a few literatures demonstrated the advances of heteroatom dopants at atomic scale, [9,10] hardly any of them focused on the atomic structure of excess doping and its mechanism of deactivation, which is also important for rational design of ideal doped photocatalysts.

In this regard, using the few-layer Cu-doped ternary sulfide ZnIn₂S₄ (ZIS), (a highly active photocatalyst) as the

Dr. P. Wang, Prof. H. Wang, Prof. S. Zhan MOE Key Laboratory of Pollution Processes and Environmental Criteria Tianjin Key Laboratory of Environmental Remediation and Pollution Control

College of Environmental Science and Engineering Nankai University

Tianjin 300350, P. R. China

E-mail: sihuizhan@nankai.edu.cn

Prof. Z. Shen Key Laboratory of Advanced Ceramics and Machining Technology Ministry of Education School of Materials Science and Engineering

Tianjin University Tianjin 300072, P. R. China

> The ORCID identification number(s) for the author(s) of this article can be found under https://doi.org/10.1002/adfm.201807013.

DOI: 10.1002/adfm.201807013

Prof. Y. Xia School of Chemistry and Chemical Engineering **Shandong University** Jinan 250100, P. R. China Dr. L. Zheng Beijing Synchrotron Radiation Facility Institute of High Energy Physics Chinese Academy of Sciences

Beijing 100049, P. R. China Dr. W. Xi School of Materials Science and Engineering Tianjin University of Technology Tianjin 300384, P. R. China



www.afm-iournal.de

example,[7,10,12,13] we have demonstrated the structural and functional characteristic for optimum and excess doping at atomic scale. Combining with the results of multiple spectroscopic analysis and theoretical simulations, it is shown that: (i) With doping quantity of 0.5 wt%, Cu atoms substitute Zn atoms in the ZIS with the metal-S4 coordination well maintained, that is, the symmetry of crystalline cell hardly changed. This probably reduces the structural combination centers. Moreover, this substitution brings an acceptor state close to the valence band (VB) maximum, which greatly increases the carrier density and charge transport efficiency and bring a superior H₂ evolution rate (four times higher than that of ZIS). (ii) With the increasing of doping quantity, the activity of photocatalyst gradually declined. When the doping quantity reaches 3.6 wt%, its activity is even worse than that of pristine ZIS. The Cu can still substitute the Zn atoms, but shows the Cu-S_{3,6} coordination with a distorted crystalline cell. This brings more structural combination centers and a low carrier density. Besides, the excess doping makes the VB maximum largely upshift of ≈1 eV, which also probably facilitate the relaxation of electrons and charge recombination. The strong photoluminescence (PL) emission and short carrier lifetime thereafter confirmed the existence of heavy charge recombination. This work brings an atomic insight for understanding the optimum and excess doping characteristic for photocatalysts. Besides, the fewlayer Cu_{0.5}-ZIS with high activity can also inspire the further development of highly efficient ultrathin 2D photocatalysts.

2. Results and Discussion

Few-layer pristine ZIS and copper-doped ZIS (Cux-ZIS) nanosheets were synthesized by a solvothermal method. The weight percentage of Cu was determined by the inductively coupled plasma (ICP) technique (Table S1, Supporting Information). Among, ZIS, Cu_{0.5}-ZIS, and Cu_{3.6}-ZIS (Cu atoms of 0.5 and 3.6 wt%, respectively) were chosen to study the atomic origin of optimum and excess doping. The transmission electron microscopy (TEM) images show that ZIS and Cu_x-ZIS nanosheets are with lateral size of 100 to several hundreds of nanometers (Figure S1, Supporting Information), and they are confirmed to be hexagonal ZnIn₂S₄ without any impurity phase (JCPDS Card No. 72-0773)[14] (Figure S2, Supporting Information), indicating the Cu_x-ZIS samples still retain the pristine crystal structure of ZIS. Furthermore, atomic force microscopy (AFM) measurements in **Figure 1**a,b and Figure S3 (Supporting Information) clearly show that the average thickness of the samples is about 5.27 nm, which corresponds to the thickness of four unit cell ZIS slab (Figure 1g). As a consequence, it is verified that clean and freestanding few-layer Cux-ZIS nanosheets are successfully synthesized. Then, high-resolution TEM (HRTEM) images (Figure 1c, and Figure S4a,c, Supporting Information) reveal the 0.33 nm interplanar distances in all of the samples matching well with the d_{100} spacings of ZIS, and the interaxial angles of 120° are also consistent with its hexagonal phase. For Cu_{0.5}-ZIS, the high-resolution high-angle annular dark-field scanning transmission electron microscopy (HAADF-STEM) image shows that its lattice is composed of hexagonal alternating zinc and sulfur sites (Figure 1d). Notably, although the

STEM-energy dispersive X-ray (EDS) mapping (Figure 1e,f and Figures S4–S6, Supporting Information) shows a uniform doping of Cu atoms for both Cu_{0.5}-ZIS and Cu_{3.6}-ZIS,^[15] different influence of Cu dopants on their atomic structure have been observed. Both ZIS and Cu_{0.5}-ZIS reveal a relatively regular atomic arrangement in the crystal lattice (Figure S7a, Supporting Information and Figure 1c), while a slight twist is observed in some regions for Cu_{3.6}-ZIS (Figure S7c, Supporting Information), indicating its distorted atomic structure. Moreover, the fast Fourier transformation (FFT) has been conducted (Figure 1h, and Figure S7b,d, Supporting Information), and the deviation of plots compared with that of ZIS further proves its subtle atomic distortion.^[16,17]

To study the chemical environment of doped Cu atoms, techniques toward subtle atomic structure analysis were employed, including X-ray absorption near edge structure (XANES), extended X-ray absorption fine structure (EXAFS), and X-ray photoelectron spectroscopy (XPS) (Figure 2a-d, Table 1, and Figure S8, Supporting Information). As shown in the XANES spectra (Figure 2a), the features of the Cu K-edge in ZIS (≈8988 eV) are close to those of Cu_{0.5}-ZIS and Cu_{3.6}-ZIS. Compared with those of Cu foil and Cu2S, the K-edge of the Cu dopant is slightly shifted to a higher energy, close to that of CuS. Therefore, the species of Cu dopants in Cu_{0.5}-ZIS and Cu_{3.6}-ZIS is Cu²⁺ rather than metallic Cu⁰ and Cu⁺. This is consistent with the results of XPS measurements (Figure S8, Supporting Information). Then, the coordination environment of Cu dopants is confirmed by Fourier transforms of EXAFS in Figure 2b. Results show that the peak positions of the Cu dopants (≈1.8 Å) for different doping levels are very similar to that of the Cu atoms in CuS, but different from Cu₂S, indicating a Cu-S bonding similar to that of CuS. However, in Figure 2c, the Cu K-edge oscillation curves for Cu_{0.5}-ZIS and Cu_{3.6}-ZIS display remarkable differences in comparison with both CuS and Cu₂S, excluding the existence of CuS and Cu2S crystallites, which is in accordance of X-ray diffraction (XRD) analysis (Figure S2, Supporting Information). In this case, Cu atom can substitute Zn or In atoms to form a Cu-S bond. To further determine the favorable atomic substitutional form of Cu in ZIS, the formation energy $(E_{\rm s})$ for defected structure was calculated. As can be seen from Figure 2d, it shows a lower E_s (1.316 eV) in the case of Cu substitutes Zn, compared to that of Cu substitutes In. Thus, Cu atom substitutes Zn atom to form a Cu-S bond. And this can be further confirmed by ICP analysis (Table S2, Supporting Information), which shows that the weight percent of Zn decreases rapidly, while the weight percent of In remains the same. Moreover, EXAFS fitting is performed to obtain the quantitative structural configuration of Cu in Cu_{0.5}-ZIS and Cu_{3.6}-ZIS. As shown in Figure 2e,f, both of their Fourier transformed EXAFS spectra can be well fitted with the proposed configuration. Table 1 summarizes the fitting parameters at the Cu K-edge for different samples. Results show that the Cu_{0.5}-ZIS well maintains the metal-S₄ coordination like that of pristine ZIS. While the Cu_{3.6}-ZIS displays a Cu-S_{3.6} coordination region similar to that of CuS (Cu-S_{3.5}). Considering the crystalline CuS impurity is excluded by XRD and Cu K-edge oscillation, this possibly suggests a distorted atomic structure in the Cu_{3.6}-ZIS. These are consistent with their results of HRTEM and XPS analysis in Figure 1, and Figures S7 and S8 (Supporting Information).

www.afm-journal.de

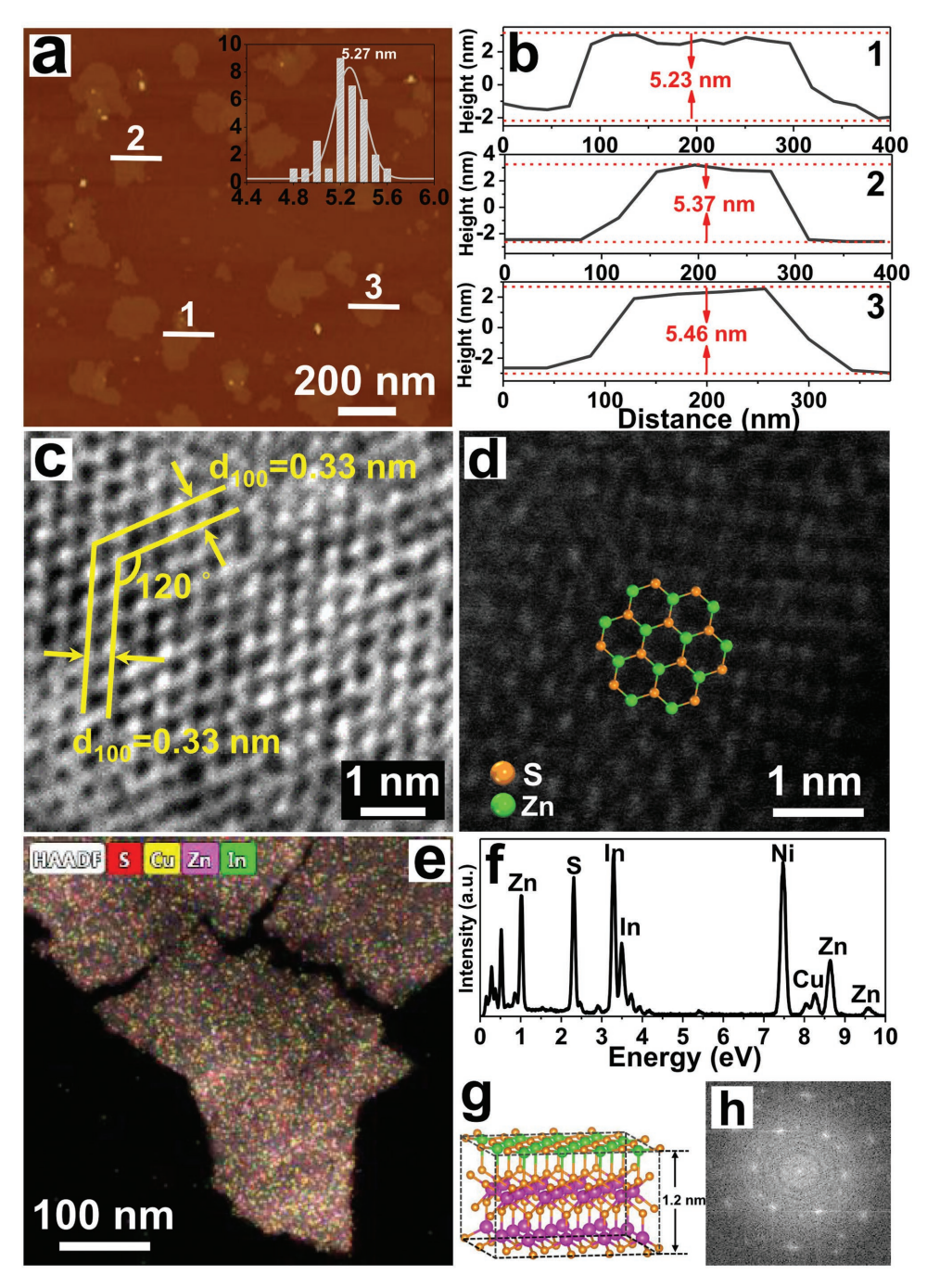


Figure 1. a) AFM image and b) the corresponding height profiles of lines 1, 2, and 3 in (a), c) high-resolution TEM image, d) high-resolution HAADF-STEM image, e) STEM-energy dispersive X-ray (EDS) mapping, f) EDS spectrum, g) 3D model of the standard unit cell, and h) fast Fourier transform image of Cu_{0.5}-ZIS.

To further evaluate the crystalline distortion extent of $\text{Cu}_{0.5}$ -ZIS and $\text{Cu}_{3.6}$ -ZIS, the Rietveld analysis of XRD and Raman spectra is performed (**Figure 3a**,b). Figure 3a shows the structure information and refined patterns of ZIS, $\text{Cu}_{0.5}$ -ZIS, and $\text{Cu}_{3.6}$ -ZIS from analyzing the XRD patterns via the Rietveld method. It is observed that the doping Cu into ZIS reduces the peak intensity, which is ascribed to smaller ionic radius of Cu^{2+} than those of Zn^{2+} , and this may lead to structural deformation in ZIS lattice. [18] Compared with those of ZIS, the c/a value

(6.488) of $\text{Cu}_{0.5}\text{-ZIS}$ is close to that of pristine ZIS (6.428), while for $\text{Cu}_{3.6}\text{-ZIS}$, its c/a value (6.349) largely deviates from those of $\text{Cu}_{0.5}\text{-ZIS}$ and pristine ZIS. This result suggests that the $\text{Cu}_{3.6}\text{-ZIS}$ has larger distortion content than that of $\text{Cu}_{0.5}\text{-ZIS}$ and consistent with the observation of HRTEM image (Figure 1c, and Figure S7a,c, Supporting Information). These phenomena can be ascribed to the lopsided Coulomb force generated by foreign metal atoms (Cu) with similar atomic radius and electron configuration. [19] Furthermore, Figure 3b shows the Raman

www.afm-journal.de

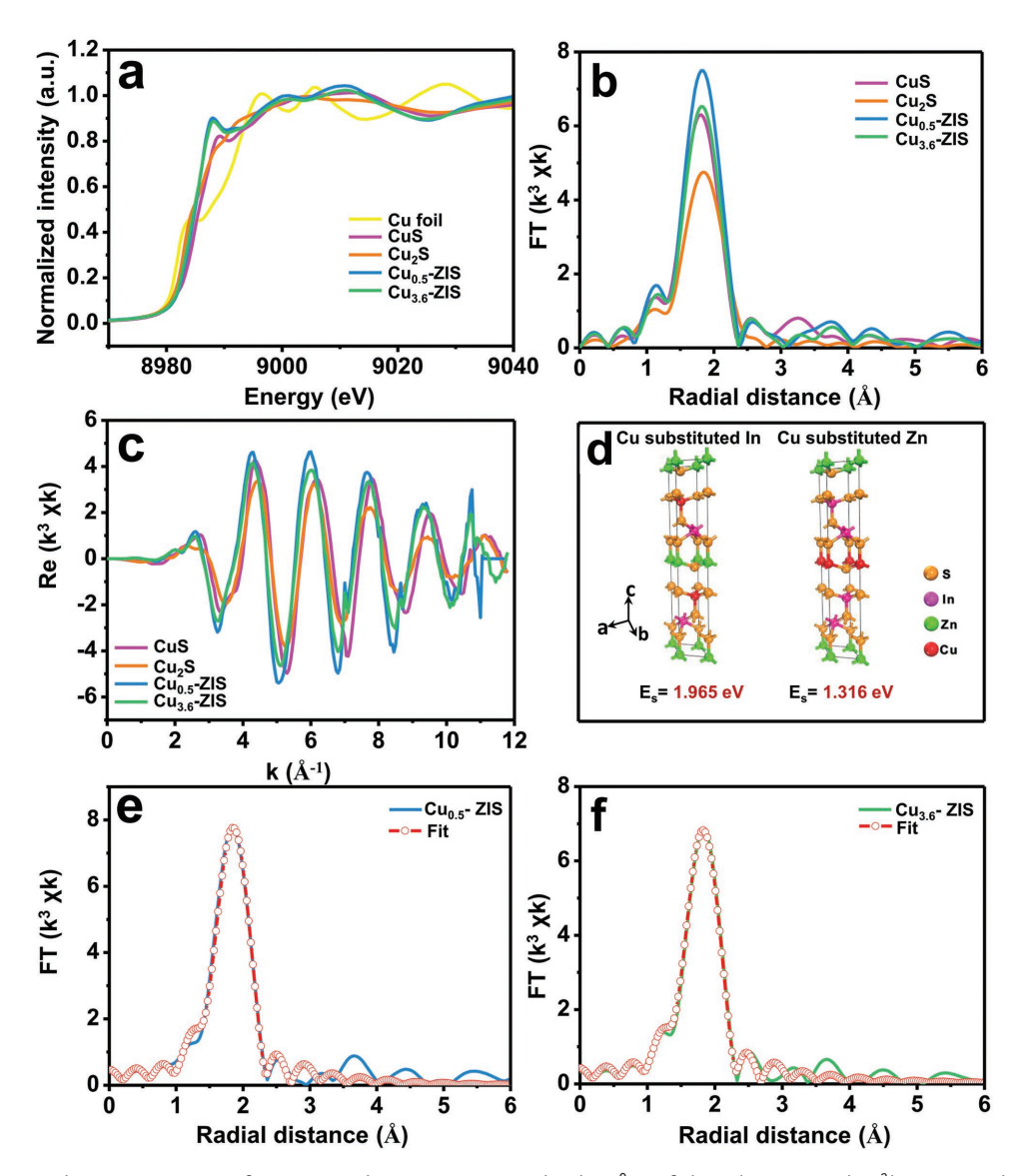


Figure 2. a) Copper K-edge XANES spectra of $Cu_{0.5}$ -ZIS and $Cu_{3.6}$ -ZIS compared with Cu^0 (Cu foil), Cu^+ (Cu_2S), and Cu^{2+} (CuS) standards. b) Magnitude of the Fourier transforms of k^3 -weighted Cu K-edge EXAFS functions in $Cu_{0.5}$ -ZIS, $Cu_{3.6}$ -ZIS, Cu_{3

vibrational modes located at around 250, 301, 346, and 370 cm⁻¹, which are attributed to the longitudinal optical mode (LO₁), transverse optical mode (TO₂), longitudinal optical mode (LO₂), and A_{1g} mode of crystalline ZIS.^[20] Compared to ZIS, no additional peaks can be detected in Cu_{0.5}-ZIS, further excluding

Table 1. EXAFS fitting parameters at the Cu K-edge for different samples.

Sample	Shell	N ^{a)}	R ^{b)} [Å]	$\sigma^{2c)}$ [Å $^2 \times 10^3$]	$\Delta E_0^{d)}$ [eV]
Cu _{0.5} -ZIS	Cu-S	4.3	2.31	8.6	4.3
Cu _{3.6} -ZIS	Cu-S	3.6	2.30	8.2	3.6
CuS	Cu-S	3.5	2.26	8.7	3.4

^{a)}Coordination numbers; ^{b)}Bond distance; ^{c)}Debye–Waller factors; ^{d)}The inner potential correction.

other crystalline impurity. However, the peak LO_1 in $Cu_{0.5}$ -ZIS shifts to lower frequency and all the peaks are comparatively weaker, indicating a decreasing crystalline symmetry compared with that of pristine ZIS. While for $Cu_{3.6}$ -ZIS, these four peaks further reduce and can hardly be observed in Figure 3b and Figure S9 (Supporting Information), indicating its further distorted atomic structure.

To verify the relationship of atomic structure–activity, the photocatalytic hydrogen evolution is chosen here as the model reaction for ZIS and Cu-doped ZIS (Figure 4). The continuous hydrogen production profile and the hydrogen production rate for different samples using the full solar spectrum are shown in Figure 4a,b, respectively. The hydrogen production rate significantly increases with Cu doping from 0.1 to 0.5 wt%, and a maximum 26.2 mmol $h^{-1}\ g^{-1}$ is observed for Cu_{0.5}-ZIS. This

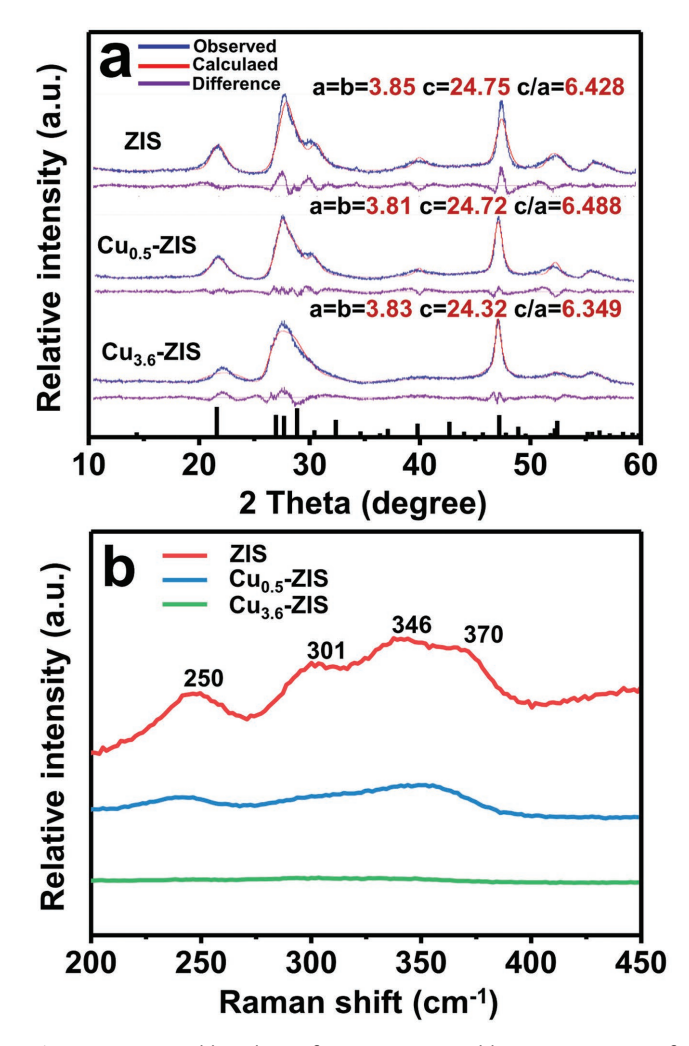


Figure 3. a) Rietveld analysis of XRD patterns and b) Raman spectra of ZIS, $Cu_{0.5}$ -ZIS and $Cu_{3.6}$ -ZIS.

hydrogen production rate is really remarkable and is four times higher than that of pristine ZIS (6.5 mmol h⁻¹ g⁻¹). However, with further increasing of the Cu doping quantity, the hydrogen evolution gradually decreases with a lowest value for the Cu_{3.6}-ZIS (0.9 mmol h⁻¹ g⁻¹). Similar activity trend can also be observed without cocatalyst or under the visible light irradiation (Figure S10, Supporting Information). Then, the quantum efficiency (QE) of Cu_{0.5}-ZIS was also calculated and provided in Figure 4c. The trend in QE closely follows that of the absorbance measured by ultraviolet-visible spectroscopy, and a relatively high OE of 4.76% at 420 nm is obtained. Besides its outstanding photocatalytic activity, Cu_{0.5}-ZIS also exhibits remarkable stability (Figure S11, Supporting Information). Furthermore, the photocatalytic activity trend can also be confirmed by the photoelectrochemical (PEC) measurements. As shown in Figure 4d, the transient photocurrent curves (TPC) manifest that the photocurrent over Cu_{0.5}-ZIS is the highest, while the photocurrent over Cu_{3.6}-ZIS is the lowest. On the basis of photocatalytic measurements, we can further confirm that the optimal amount of Cu doping is 0.5 wt%, while the excess doping of 3.6 wt% is harmful for the activity. Combining with the analysis results of their microstructure (Figures 1–3), it can be inferred that this activity trend highly depends on their different atomic structure and corresponding charge transport behavior, which will be demonstrated as follows.

Therefore, to further elucidate the functional mechanism of optimum and excess doping for Cu-doped ZIS, multiple methods have been used including theoretical simulations, electrochemical and spectroscopic techniques (Figure 5). For Cu_{0.5}-ZIS, to explore why 0.5 wt% Cu doping can promote hydrogen production of ZIS, the theoretical investigations have been first conducted, using one Cu atom substitutes the Zn atom in the slab (0.9 wt% Cu) (Figures S12 and S13, Supporting Information). As shown in Figure 5a,b, after Cu doping, the intrinsic bandgap of ZIS has been narrowed. Thus, it can be speculated that the absorption edge of Cu-doped ZIS redshifts to longer wavelength, which is consistent with the ultraviolet-visible diffuse reflectance spectra (Figures S14 and S15, Supporting Information). However, the contribution of hydrogen evolution rate under long wavelength monochromatic light to total production is a quite minor part (Table S3, Supporting Information). Thus, in our case, the superior hydrogen evolution rate of Cu_{0.5}-ZIS should mainly be attributed to enhanced charge separation/transfer. As shown in the calculated density of states (DOS), the hybridization leads to some states passing through the Fermi level, which act as electronic acceptor states. These unfilled acceptor states close to the VB maximum induce the metallic conductive characters of simulated Cu-doped ZIS, and the elevation of E_f level indicates the separation of carriers has been effectively enhanced.^[21] Furthermore, the electron difference density analysis of simulated Cu-doped ZIS in Figure 5c shows that the delocalized Cu 3d states is beneficial for the migration of charge carriers, indicating that the Cu_{0.5}-ZIS nanosheets could provide more charge carriers that can participate in the catalytic reaction, which helps to significantly improve their photocatalytic performances.^[22] Thereafter, photoluminescence spectra are used to examine the efficiency of charge separation and lifetime of photogenerated charges (Figure 5d,e). As shown in Figure 5d, all samples show two emission peaks, the emission peak around 425 nm is assigned to some defects (e.g., sulfur and zinc vacancy), while the emission peak centered at 520 nm is derived from band-to-band transition.^[23,24] Compared with ZIS, Cu_{0.5}-ZIS shows a much lower PL peak intensity, suggesting a suppressed photogenerated charge recombination induced by enhanced charge transport, which is consistent with the density functional theory (DFT) calculations. Thus, the acceptor states induced by optimal Cu doping do not act as a recombination center, but serve as the separation centers to capture the photogenerated electrons.[9] Furthermore, the charge carrier lifetimes of the samples are also evaluated and Cu_{0.5}-ZIS shows the longest lifetime (9.59 ns), indicating more photogenerated electrons/holes can participate in the reaction than those of ZIS and Cu_{3.6}-ZIS (Figure 5e). While for Cu_{3.6}-ZIS, its two peaks in PL spectra have a slight blueshift, which suggests an enhanced Burstein-Moss effect in ZIS doped with higher Cu2+ concentrations.[25] Furthermore, it shows the strongest PL peak, indicating a serious emission type charge recombination, which can be ascribed to the structural combination sites brought by its distorted atomic

www.advancedsciencenews.com www.afm-journal.de

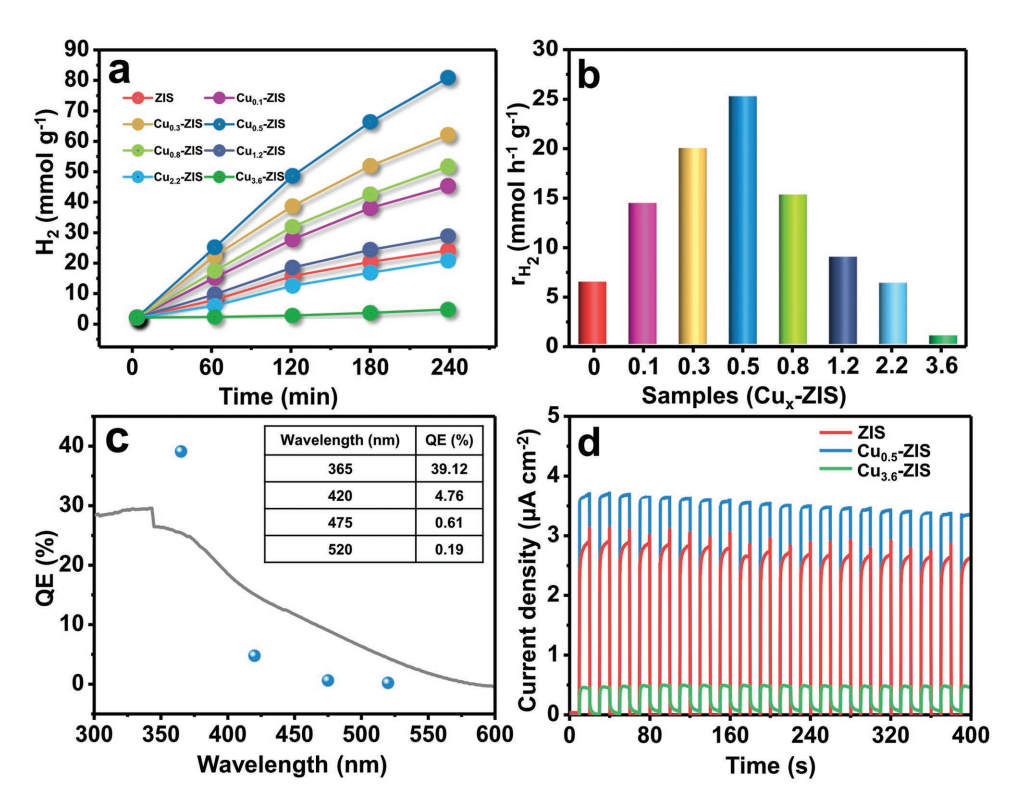


Figure 4. a) H_2 generation profile and b) rate (r_{H2}) of ZIS and Cu-ZIS samples. c) QE of Cu_{0.5}-ZIS at 365, 420, 475, and 520 nm. d) TPC responses of ZIS, Cu_{0.5}-ZIS, and Cu_{3.6}-ZIS samples.

structure. Moreover, excess Cu doping into ZIS lattice results in a largely upshift of VB maximum (Figure S16, Supporting Information), which probably makes it much easier to realize the combination of holes and electrons from the bottom of the conduction band.^[26] Furthermore, Cu_{3.6}-ZIS exhibits the shortest lifetime (1.02 ns), indicating fewest electron/holes can participate in the reactions, and consistent with its lowest photocatalytic activity.

To further uncover the correlation between the amount of Cu doping and electron–hole separation efficiency of the Cu-doped ZIS, surface photovoltage spectroscopy (SPV) was conducted, which can show the carrier separation and transportation behaviors. [14] In Figure 5f, all the samples display an obvious SPV response from 300 to 550 nm, with a main SPV peak at about 375 nm, which is mainly attributed to the band-to-band electronic transition. [27] Obviously, Cu_{0.5}-ZIS exhibits a higher SPV response than ZIS, indicating the charge separation has been increased via the effective diffusion process since its builtin electric field is usually neglected, hence favoring a higher photocatalytic activity. [28] However, Cu_{3.6}-ZIS shows a very low SPV response, indicating the generated electron–hole pairs are difficult to separate, thus weakening its activity. This is consistent with the result of its PL spectra.

Furthermore, to obtain a deep insight into the charge transport behavior in the absence of light excitation, electrochemical impedance spectra (EIS) and Mott–Schottky measurements were carried out under dark conditions. As can be seen from **Figure 6a**, the EIS Nyquist plots of ZIS, $Cu_{0.5}$ -ZIS, and $Cu_{3.6}$ -ZIS are well simulated to the equivalent electrical circuit (Figure 6a inset), in which $R_{\rm s}$ and $R_{\rm t}$ are the electrolyte solution

resistance and the interfacial charge-transfer resistance, respectively. [29] Based on the above model, $Cu_{0.5}$ -ZIS shows a much smaller semicircle diameter and a much lower R_t value than ZIS, suggesting its lower interfacial charge-transfer resistance from electrode to electrolyte molecules. However, Cu_{3.6}-ZIS shows the highest diameter and Rt value, suggesting its highest resistance for charge transfer. To further understand and retrieve quantitative insight about the charge carrier density of Cu-doped ZIS, the capacitance measurement on the electrode/electrolyte was conducted. Figure 6b shows the Mott-Schottky plots as $1/C^2$ versus potential, all the samples show positive slopes, suggesting they are n-type semiconductors with electrons as major carriers. The linear parts of the curves are extrapolated to $1/C^2 = 0$, the values of $E_{\rm fb}$ are estimated to be -1.06, -1.09, and -1.04 eV for ZIS, $Cu_{0.5}$ -ZIS, and $Cu_{3.6}$ -ZIS, respectively. Then, the calculated carrier densities (Section S1, Supporting Information)[30] of ZIS, Cu_{0.5}-ZIS, and Cu_{3.6}-ZIS are 1.18×10^{19} , 2.64×10^{19} , and 4.39×10^{18} cm⁻³, respectively. The electron density of Cu_{0.5}-ZIS is about two times higher than ZIS, suggesting a much faster carrier transfer in Cu_{0.5}-ZIS. This further confirms its DFT results. In contrast, Cu_{3.6}-ZIS exhibits the lowest electron density.

Consequently, combined with the above measurements, it is deemed that the optimal Cu doping (0.5 wt% in our case) for ZIS completely optimize the vital processes in photocatalytic hydrogen evolution. However, the distorted atomic structure and largely upshift of VB maximum induced by excess Cu doping will dramatically reduce the photocatalytic activity. Finally, a possible photocatalytic schematic diagram of Cu-ZIS is illustrated in Figure S17 (Supporting Information).

www.advancedsciencenews.com www.afm-journal.de

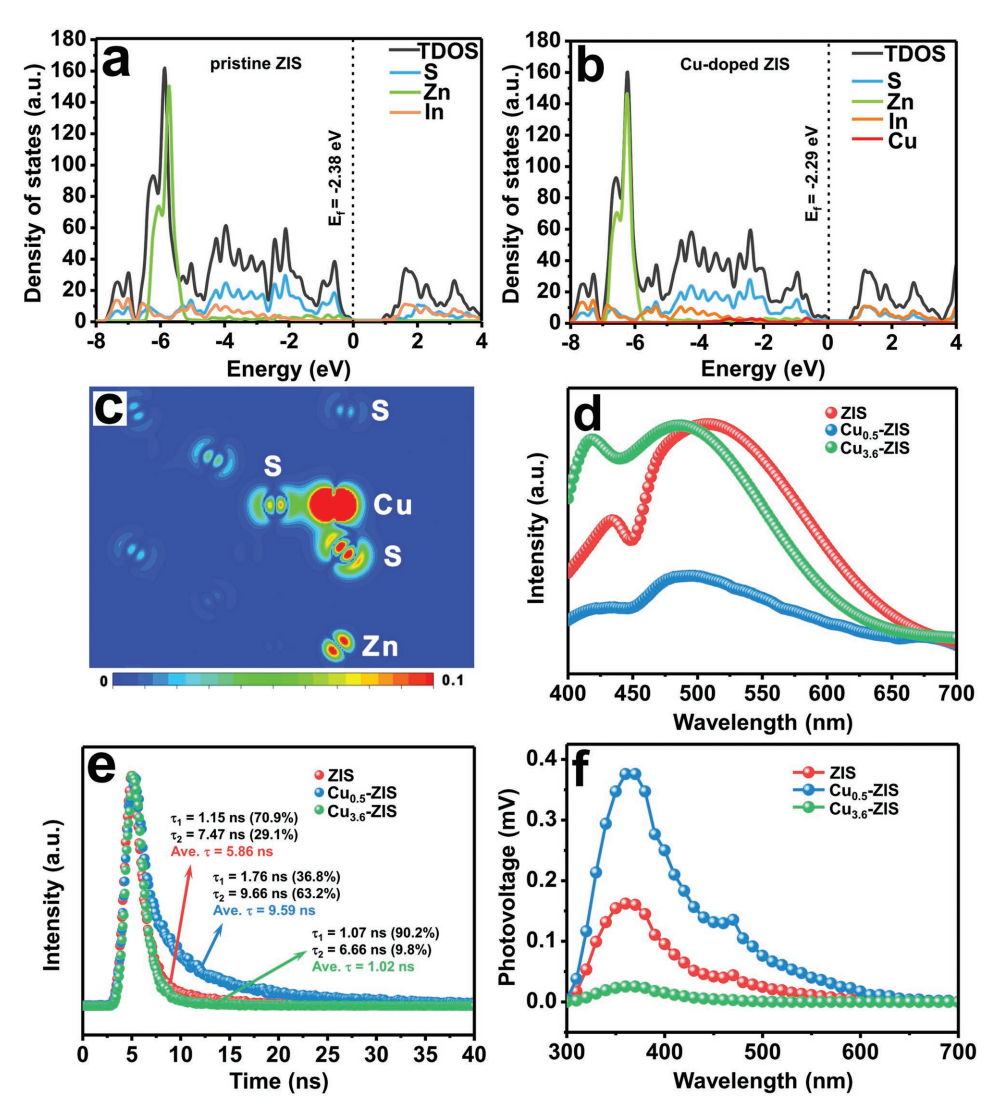


Figure 5. Calculated density of states (DOS) of a) ZIS slab and b) Cu-ZIS slab. E_f = Fermi level. c) The electron difference density analysis of Cu-ZIS. d) Steady-state PL spectra, e) time-resolved PL decay spectra, and f) SPV spectra of ZIS, Cu_{0.5}-ZIS, and Cu_{3.6}-ZIS.

3. Conclusion

In summary, we built a model of few-layer Cu-ZIS nanosheets and hence disclose the optimum and excess doping structure at

atomic scale, with efforts to uncover the relationship between structure and photocatalytic performance. With the optimal doping concentration, the $\text{Cu}_{0.5}$ -ZIS exhibits the hydrogen evolution rate of 26.2 mmol h⁻¹ g⁻¹ and a high QE of 4.76% at

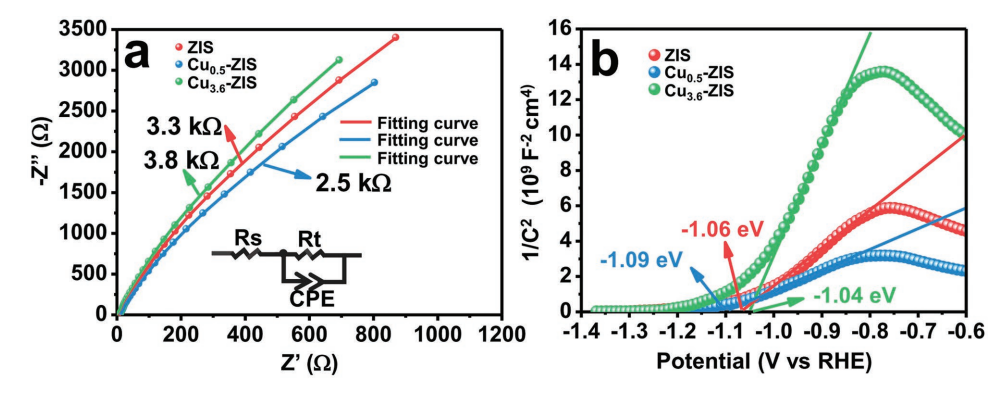


Figure 6. a) EIS Nyquist plots and b) Mott-Schottky plots of ZIS, Cu_{0.5}-ZIS, and Cu_{3.6}-ZIS.

www.afm-journal.de

420 nm, which is really remarkable and four times higher than that of pristine ZIS (6.5 mmol h⁻¹ g⁻¹). These can be ascribed to (i) its well-maintained metal-S₄ coordination, negligible distorted structure, and thus reduced structural combination sites; (ii) unfilled acceptor states in the VB top that can effectively enhance the separation of carriers and suppress the undesirable recombination as revealed by DFT calculations. In contrast, the Cu_{3.6}-ZIS, which possess excess Cu dopants, exhibited even lower activity than that of ZIS (0.9 mmol h⁻¹ g⁻¹). It is proposed that the distorted atomic structure and largely upshift of VB maximum induced by newly formed Cu-S_{3.6} coordination may contribute to the heavy electron-hole recombination. This work studies the atomic origin of optimum and excess doping for photocatalyst, which will inspire the rational doping engineering. Besides, the excellent performance of Cu_{0.5}-ZIS nanosheets will promote the development of highly active ultrathin 2D photocatalysts.

4. Experimental Section

Preparation of ZnIn₂S₄ and Cu-Doped ZnIn₂S₄ Ultrathin Nanosheets: For a typical preparation of ZnIn₂S₄ ultrathin nanosheets, 0.8 mmol Zn(CH₃COO)₂·2H₂O, 1.6 mmol InCl₃·4H₂O, and 6.4 mmol thioacetamide were dissolved in 30 mL water and 30 mL ethanol with vigorous stirring for 30 min. The resulting mixture was then sealed in a 100 mL stainless steel autoclave, heated to 180 °C, and maintained for 24 h. After cooling to room temperature naturally, the obtained products were collected by centrifugation, washed with ethanol and distilled water, and then dried at 60 °C in air overnight for further characterization. The ZnIn₂S₄ is denoted as ZIS. To prepare Cu-doped ZnIn₂S₄ ultrathin nanosheets, 0.2, 0.4, 0.6, 0.8, 1, 2, and 3 mL 0.1 M Cu(NO₃)₂ solution were added into the mixed solution before transferring into the autoclave. The mass fractions of Cu in Cu-ZIS were determined by ICP-MS (Table S1, Supporting Information). And the obtained products are denoted as Cu_{0.1}-ZIS, Cu_{0.3}-ZIS, Cu_{0.5}-ZIS, Cu_{0.8}-ZIS, Cu_{1.2}-ZIS, $Cu_{2.2}$ -ZIS, and $Cu_{3.6}$ -ZIS, respectively.

Characterizations: XRD patterns were recorded on Rigaku D/Max 2200 PC X-ray diffractometer with Cu K α radiation (λ = 0.15418 nm). Scanning electron microscopy (SEM) and elemental mapping images were performed using a Hitachi SU8010 at an accelerating voltage of 3 kV (Japan). TEM and HRTEM analyses were conducted using a JEOL JEM-2100F at an accelerating voltage of 200 kV (Japan). The HAADF images and elemental mapping results were obtained using the STEM mode of an FEI Titan Themis G1 with double aberration correctors and four EDS detectors, each of which had an active area of 30 mm² for detecting the EDS signals. Tapping-mode AFM images were performed by using a Bruker's Dimension Icon Atomic Force Microscope System. Determination of the metal elements content was undertaken by means of ICP-MS (X7 Series, Thermo Electron Corporation, USA). XPS measurements were performed in a Thermal ESCALAB 250 electron spectrometer using Al Klpha radiation X-ray source (hv = 1486.6 eV) to determine the valence states of all elements. UV-vis diffused reflectance spectra of the samples were obtained using a Shimadzu Corporation UV-vis spectrophotometer to record the absorption spectra of the samples. Steady-state PL spectra were measured using an Edinburgh Instruments FLS920P equipped with a Xe lamp-920 at room temperature under the excitation of 336 nm. Time-resolved PL decay curves were recorded on a FLS920 fluorescence lifetime spectrophotometer under the excitation of 336 nm and probed at 495 nm. The SPV spectra were obtained on a CEL-SPS1000 surface photovoltage spectrometer, which is a product of Beijing CEAULIGHT, Inc. The measurement systems include a lockin amplifier (SR830, Stanford Research Systems, Inc.), and a simple chamber. Monochromatic light was generated from a 500 W xenon

lamp (CHF-XM-500 W, global xenon lamp power) by a monochromator (Omni-3007, No. 16047, Zolix).

Photocatalytic Activity Test: The photocatalytic hydrogen production test was carried out in a closed system with a quartz flask of 150 mL. A full spectrum solar simulator (CEL-S500) with AM 1.5G filter, which was about 1 Sun power, was used to provide incident light and the area of the surface irradiated in the cylinder reactor was about 17.8 cm². In a typical photocatalytic experiment, 100 mg of photocatalyst powder was suspended with a constant stirring in 100 mL aqueous solution containing 20% 0.75 M ascorbic acid as sacrificial electron donor. 1 wt% Pt was deposited onto the surface of photocatalysts by the in situ photodeposition method using H₂PtCl₆ under solar simulator for 30 min. Then the reaction system was thoroughly degassed by evacuation. Next, the mixture was illuminated under continuous magnetic stirring and a water-cooling filter was used to keep the reaction temperature at ≈10 °C. The generated gas spread into the quantitative loop (1 mL) of a six-way valve, and the gas volume was analyzed by gas chromatography equipped with a thermal conductive detector every 60 min to determine the hydrogen generation rate.

The apparent QE at a wavelength of 365, 420, 475, and 520 nm was measured under the identical reaction condition by placing various band-pass filters in front of the light source. The CEL-NP2000 spectroradiometer was used to measure the intensity of the incident light. The apparent QE was calculated according to the following equation^[31]

$$AQE[\%] = \frac{Number of reacted electrons}{Number of incident photons} \times 100$$
 (1)

X-Ray Absorption Fine Structure: The X-ray absorption find structure spectra (Fe K-edge) were collected at 1W1B station in Beijing Synchrotron Radiation Facility (BSRF). The storage rings of BSRF were operated at 2.5 GeV with a maximum current of 250 mA. Using Si (111) double-crystal monochromator, the data collection was carried out in transmission mode using ionization chamber. All spectra were collected in ambient conditions.

The acquired EXAFS data were processed according to the standard procedures using the ATHENA module implemented in the IFEFFIT software packages. [32] The k^3 -weighted EXAFS spectra were obtained by subtracting the post-edge background from the overall absorption and then normalizing with respect to the edge-jump step. Subsequently, k^3 -weighted $\chi(k)$ data of Cu K-edge were Fourier transformed to real (R) space using a Hanning windows ($dk = 1.0 \ \mathring{A}^{-1}$) to separate the EXAFS contributions from different coordination shells. To obtain the quantitative structural parameters around central atoms, least-squares curve parameter fitting was performed using the ARTEMIS module of IFEFFIT software packages.

Theoretical Calculation: Spin-polarized calculations were performed using the Vienna ab initio simulation package (VASP). [33,34] The exchange-correction function was treated by the Perdew–Burke–Ernzerhof for solid (PBEsol) generalized gradient approximation (GGA) [35] and the wavefunctions were expanded in a plane wave basis with an energy cutoff of 500 eV. The (110)-oriented ZnIn2S4 single layers were simulated by periodically repeating the four atomic layers along the [110] direction of the unit cell. Each ZnIn2S4 single-layer model consists of eight atomic planes and is separated by a vacuum region of 15 Å. A 2×2 2D unit cell was used to simulate the ZnIn2S4 single-layer model, two Zn atoms coordinated by S atoms were replaced by Cu atoms in each of the two four-atomic ZnIn2S4 layers along the [110] direction. All self-consistent field (SCF) calculations were converged to 10^{-5} eV and the forces are smaller than 0.02 eV Å $^{-1}$.

To further determine the favorable atomic substitutional form of Cu in ${\rm ZnIn_2S_4}$, the formation energy $E_{\rm s}$ for defected structure is calculated as follows

$$E_{s} = E_{ZIS-d} + \mu_{d} - (E_{ZIS} + \mu_{Cu})$$
 (2)



www.afm-journal.de www.advancedsciencenews.com

where E_{ZIS} and E_{ZIS-d} are the energies for pristine $ZnIn_2S_4$ and structure with defects, respectively. The chemical potentials of substituted atoms (d) and Cu atom are derived from the bulk phase.

Photoelectrochemical Activity Test: The working photoanodes were fabricated as follows: 4 mg sample, 1 mL ethanol, and 20 µL Nafion were mixed by sonication for 30 min to make a slurry. The slurry was then dropped onto an indium-tin oxide (ITO) glass. After the ethanol evaporated thoroughly at ambient temperature, the photoanodes were dried at 60 °C for 8 h. The active areas of the photoanodes are \approx 2.75 cm². PEC performances of the prepared photoanodes were recorded on an electrochemical work station (CHI660E Instruments) with a standard three-electrode system (an Ag/AgCl electrode reference electrode and a Pt foil counter electrode). 0.5 M Na₂SO₄ solution was used as the electrolyte. The measured potential versus Ag/AgCl was converted to reversible hydrogen electrode (RHE) scale using the Nernst equation: $E_{RHE} = E_{Ag/AgCl} + 0.197 + 0.059 \text{ pH}$. A 300 W Xe lamp was used as a light source. Typically, polarization curves were recorded at a scan rate of 5 mV \mbox{s}^{-1} and the chopped illumination was used to examine transient photocurrents. Transient photocurrent measurements with chopped illumination were also conducted to examine the steady-state photocurrent densities of the photoanodes. EIS was carried out in the frequency range of 0.05-105 Hz.

Supporting Information

Supporting Information is available from the Wiley Online Library or from the author.

Acknowledgements

P.W. and Z.S. contributed equally to this work. The authors gratefully acknowledge the financial support by the Natural Science Foundation of China as general projects (Grant Nos. 21722702 and 21872102), and the Tianjin Commission of Science and Technology as key technologies R&D projects (Grant Nos. 16YFXTSF00440, 16ZXGTSF00020, and 16YFZCSF00300). The authors also acknowledge Prof. J. Luo for the STEM measurements, and Dr. W. Chen for the analysis of XANES and EXAFS.

Conflict of Interest

The authors declare no conflict of interest.

Keywords

atomic insights, few-layer nanosheets, optimum and excess doping, photocatalysis

> Received: October 5, 2018 Revised: November 7, 2018 Published online: November 26, 2018

[1] R. Chattot, O. Le Bacq, V. Beermann, S. Kuhl, J. Herranz, S. Henning, L. Kuhn, T. Asset, L. Guetaz, G. Renou, J. Drnec,

P. Bordet, A. Pasturel, A. Eychmuller, T. J. Schmidt, P. Strasser, L. Dubau, F. Maillard, Nat. Mater. 2018, 17, 827.

- [2] Z. Hu, L. Yuan, Z. Liu, Z. Shen, J. C. Yu, Angew. Chem., Int. Ed.
- [3] Y. Zhao, Y. Wang, X. Liu, J. Liu, B. Han, X. Hu, F. Yang, Z. Xu, Y. Li, S. Jia, Angew. Chem., Int. Ed. 2018, 57, 5765.
- [4] J. Li, X. Wu, W. Pan, G. Zhang, H. Chen, Angew. Chem., Int. Ed. 2018, 57, 491.
- [5] K. Wenderich, G. Mul, Chem. Rev. 2016, 116, 14587.

2016. 55. 9793.

- [6] R. Asahi, T. Morikawa, T. Ohwaki, K. Aoki, Y. Taga, Science 2001,
- [7] S. Shen, L. Zhao, Z. Zhou, L. Guo, J. Phys. Chem. C 2008, 112, 16148
- [8] R. Asahi, T. Morikawa, H. Irie, T. Ohwaki, Chem. Rev. 2014, 114,
- [9] R. J. Ran, T. Y. Ma, G. Gao, X. Du, S. Qiao, Energy Environ. Sci. 2015, 8, 3708.
- [10] W. Yang, L. Zhang, J. Xie, X. Zhang, Q. Liu, T. Yao, S. Wei, Q. Zhang, Y. Xie, Angew. Chem., Int. Ed. 2016, 55, 6716.
- [11] Z. Yu, X. Q. Chen, X. Kang, Y. Xie, H. Zhu, S. Wang, S. Ullah, H. Ma, L. Wang, G. Liu, Adv. Mater. 2018, 30, 1706259.
- [12] Z. Lei, W. You, M. Liu, G. Zhou, T. Takata, M. Hara, K. Domen, C. Li, Chem. Commun. 2003, 9, 2142.
- [13] Y. Chen, R. Huang, D. Chen, Y. Wang, W. Liu, X. Li, Z. Li, ACS Appl. Mater. Interfaces 2012, 4, 2273.
- [14] X. Jiao, Z. Chen, X. Li, Y. Sun, S. Gao, W. Yan, C. Wang, Q. Zhang, Y. Lin, Y. Luo, J. Am. Chem. Soc. 2017, 139, 7586.
- [15] W. Liu, E. Hu, H. Jiang, Y. Xiang, Z. Weng, M. Li, Q. Fan, X. Yu, E. I. Altman, H. Wang, Nat. Commun. 2016, 7, 10771.
- [16] P. Y. Huang, C. S. Ruizvargas, V. D. Z. Am, W. S. Whitney, M. P. Levendorf, J. W. Kevek, S. Garg, J. S. Alden, C. J. Hustedt, Y. Zhu, Nature 2011, 469, 389.
- [17] A. M. V. D. Zande, P. Y. Huang, D. A. Chenet, T. C. Berkelbach, Y. M. You, G. H. Lee, T. F. Heinz, D. R. Reichman, D. A. Muller, J. C. Hone, Nat. Mater. 2013, 12, 554.
- [18] K. C. Verma, R. K. Kotnala, Appl. Phys. 2016, 16, 175.
- [19] Y. Liu, X. Hua, C. Xiao, T. Zhou, P. Huang, Z. Guo, B. Pan, Y. Xie, J. Am. Chem. Soc. 2016, 138, 5087.
- [20] S. Shen, L. Zhao, L. Guo, J. Phys. Chem. Solids 2008, 69, 2426.
- [21] M. Dong, P. Zhou, C. Jiang, B. Cheng, J. Yu, Chem. Phys. Lett. 2017, 668.1
- [22] X. D. Zhang, X. Xie, H. Wang, J. J. Zhang, B. C. Pan, Y. Xie, J. Am. Chem. Soc. 2013, 135, 18.
- [23] W. Peng, G. Cong, S. Qu, Z. Wang, Opt. Mater. 2006, 29, 313.
- [24] S. Shen, P. Guo, L. Zhao, Y. Du, L. Guo, Cheminform 2011, 42, 2250.
- [25] Q. C. Sun, L. Yadgarov, R. Rosentsveig, G. Seifert, R. Tenne, J. L. Musfeldt, ACS Nano 2013, 7, 3506.
- [26] M. Cao, C. Yu, J. Xia, D. Jiang, S. Wang, H. Li, J. Am. Ceram. Soc.
- [27] Q. Li, X. Li, S. Wageh, A. A. Al-Ghamdi, J. Yu, Adv. Energy Mater. **2015**, *5*, 1500010.
- [28] Y. Luan, L. Jing, J. Wu, M. Xie, Y. Feng, Appl. Catal., B 2014, 147, 29.
- [29] J. R. Ran, J. Zhang, J. G. Yu, S. Z. Qiao, ChemSusChem 2014, 7, 3426.
- [30] Z. H. Zhang, Y. J. Yu, P. Wang, ACS Appl. Mater. Interfaces 2012, 4,
- [31] M. C. Liu, D. W. Jing, Z. H. Zhou, L. J. Guo, Nat. Commun. 2013, 4, 2278.
- [32] B. Ravel, M. Newville, J. Synchrotron Radiat. 2005, 12, 537.
- [33] G. Kresse, J. Hafner, Phys. Rev. B 1995, 48, 13115.
- [34] G. Kresse, J. Furthmüller, Comput. Mater. Sci. 1996, 6, 15.
- [35] J. P. Perdew, K. Burke, M. Ernzerhof, Phys. Rev. Lett. 1996, 77, 3865.